

The Mass of the Central Black Hole in the Seyfert Galaxy NGC 4151

Kyle G. Metzroth^{1,2}, Christopher A. Onken^{1,3}, and Bradley M. Peterson¹

ABSTRACT

In order to improve the reverberation-mapping based estimate of the mass of the central supermassive black hole in the Seyfert 1 galaxy NGC 4151, we have reanalyzed archival ultraviolet monitoring spectra from two campaigns undertaken with the *International Ultraviolet Explorer*. We measure emission-line time delays for four lines, C IV λ 1549, He II λ 1640, C III] λ 1909, and Mg II λ 2798, from both campaigns. We combine these measurements with the dispersion of the variable part of each respective emission line to obtain the mass of the central object. Despite the problematic nature of some of the data, we are able to measure a mass of $(4.14 \pm 0.73) \times 10^7 M_{\odot}$, although this, like all reverberation-based masses, is probably systematically uncertain by a factor of 3–4.

Subject headings: galaxies: active — galaxies: nuclei — galaxies: Seyfert — quasars: emission lines — ultraviolet: galaxies

1. INTRODUCTION

Reverberation mapping (Blandford & McKee 1982; Peterson 1993) of active galactic nuclei (AGNs) is used to characterize the size of the broad-line region (BLR) in these objects by measuring the time delay between continuum changes and the response of the emission lines. By combining the reverberation time delay, or “lag,” with the width of the variable part of the emission line, it is possible to estimate the mass of the central object, presumably

¹Department of Astronomy, The Ohio State University, Columbus, OH 43210; peterson@astronomy.ohio-state.edu

²Current address: Department of Mechanical Engineering, The Ohio State University, 650 Ackerman Road, Columbus, OH 43202; metzroth.1@osu.edu

³Current address: NRC Herzberg Institute of Astrophysics, 5071 West Saanich Road, Victoria, BC V9E 2E7, CANADA; Christopher.Onken@nrc-cnrc.gc.ca

a supermassive black hole, under the assumption that the dynamics of the BLR gas are dominated by gravity. In this case, the mass is given by

$$M_{\text{BH}} = \frac{f c \tau \Delta V^2}{G}, \quad (1)$$

where the size of the BLR is given by the light-travel time $c\tau$ and τ is the emission-line time delay, ΔV is the width of the emission line, G is the gravitational constant, and f is a factor of order unity that depends on the geometry, kinematics, and inclination of the BLR. Two lines of evidence argue that the reverberation-based mass estimates have some veracity:

1. Different emission lines have different response times, and these are inversely correlated with line width in a manner consistent with a virialized BLR, i.e., $\tau \propto \Delta V^{-2}$ (Peterson & Wandel 1999, 2000; Onken & Peterson 2002; Kollatschny 2003). Moreover, at least in the particularly well-studied case of the $\text{H}\beta$ line in NGC 5548, the lag and line width change over time in response to luminosity changes, and the virial relationship seems to be preserved (Peterson et al. 2004; Cackett & Horne 2006).
2. There is a relationship between the reverberation-based black hole mass M_{BH} and host-galaxy bulge velocity dispersion σ_* that is consistent with the same correlation, the $M_{\text{BH}}\text{-}\sigma_*$ relationship, that is observed in quiescent galaxies (Ferrarese & Merritt 2000; Gebhardt et al. 2000a,b; Ferrarese et al. 2001; Tremaine et al. 2002; Onken et al. 2003, 2004; Nelson et al. 2004).

With respect to the second point, the consistency of the $M_{\text{BH}}\text{-}\sigma_*$ relationship between AGNs and quiescent galaxies allows us to calibrate the reverberation-based mass scale to that of quiescent galaxies by determining a statistical mean value for the scaling constant f in eq. (1), as was done by Onken et al. (2004).

Reverberation results also show that there is a simple relationship between the size of the BLR $R = c\tau$ and luminosity L of the form $R \propto L^\alpha$, where $\alpha \approx 0.5$, but depends somewhat on the luminosity measure and also, presumably, the particular emission line for which R is measured (Kaspi et al. 2000, 2005; Bentz et al. 2006a). This is an especially important result, since the mass of the black hole in any AGN can then be estimated through a single measurement of luminosity and line width, thus enabling mass estimates for large populations of AGNs (Wandel, Peterson, & Malkan 1999; Vestergaard 2002, 2004; McLure & Jarvis 2002; Kollmeier et al. 2006; Vestergaard & Peterson 2006).

Reverberation mapping is currently the only broadly applicable method by which we can directly measure AGN black hole masses and it holds future promise because it is the only direct method of black hole mass measurement that does not depend on angular resolution.

Moreover, reverberation-based mass measurements anchor the calibration for masses based on radius–luminosity scaling relationships. Thus, given the importance of the reverberation results, we have undertaken a variety of programs designed to improve the reverberation measurements from existing data, in addition to carrying out new reverberation-mapping experiments. These efforts have included compilation and consistent reanalysis of most existing reverberation data (Peterson et al. 2004). In the particular case of NGC 3783, we completely remeasured and reanalyzed the data obtained with the *International Ultraviolet Explorer (IUE)* using improved spectral extractions (Onken & Peterson 2002), which resulted in a remarkable improvement in the precision of the central black hole mass. In this contribution, we undertake a similar reanalysis on the *IUE* spectra of NGC 4151, motivated at least in part by the fact that NGC 4151 is one of the few AGNs in which measurement of the black hole mass by other means is plausible, which would thus enable a direct comparison between masses measured by reverberation and those measured by other direct methods.

In this contribution, we re-examine spectra from two ultraviolet monitoring campaigns undertaken with *IUE* in 1988 (Clavel et al. 1990) and in 1991 (Ulrich & Horne 1996), and compare the results with those from two ground-based optical monitoring programs that were reanalyzed by Peterson et al. (2004). A third ultraviolet monitoring program on NGC 4151 in 1993 (Crenshaw et al. 1996) is not revisited here because the program was too short (9.3 days) to yield meaningful results on the emission-line responses. In section 2, we describe the processing and measurement of the ultraviolet spectra. Our reverberation analysis is described in section 3, and in section 4 we discuss our measurement of the black hole mass. Our conclusions appear in section 5.

2. THE ULTRAVIOLET SPECTRA

The databases for both *IUE* monitoring programs consist of multiple observations made with the Short Wavelength Prime (SWP) and Long Wavelength Prime (LWP) cameras in the low-dispersion mode with a large ($10'' \times 20''$) oval aperture. The SWP spectra cover the wavelength range 1150 Å to 2000 Å, while the LWP spectra cover the range 1800 Å to 3300 Å, although the LWP spectra are nearly worthless shortward of about 2200 Å. The first data set that we examine was obtained during the period 1988 November 29 to 1989 January 30 and is comprised of 33 SWP and 22 LWP spectra (Clavel et al. 1990). The second set was obtained between 1991 November 9 and December 15, and is comprised of 44 SWP and 37 LWP spectra (Ulrich & Horne 1996). The original spectral images were processed with NEWSpectral Image Processing System (NEWSIPS), replacing the older *IUE* Spectral Image Processing System (IUESIPS) extractions that were used in the original analysis. Compared

to the IUESIPS spectra, the NEWSIPS spectra have improved photometric accuracy and higher signal-to-noise ratio (S/N); AGN spectra processed with NEWSIPS show a 10%–50% increase in S/N (Onken & Peterson 2002 and references therein).

Measurements were made of each of the SWP and LWP spectra. The continuum flux was measured in the SWP spectra over a 30 Å bandpass centered on 1355 Å in the observed frame. Emission-line fluxes were measured by defining nominally line-free regions bracketing the lines, fitting a linear continuum between these regions and measuring the flux above the interpolated continuum. The wavelengths of the continuum fitting regions and the limits of the line integration are given for four emission lines, C IV λ 1549, He II λ 1640, C III] λ 1909, and Mg II λ 2798, in Table 1. We did not include measurements of the Ly α λ 1215+N V λ 1240 complex because this spectral region is hopelessly contaminated by geocoronal Ly α emission. We also attempted to measure the flux in the Si IV λ 1400 feature, but the results were very poor because the line is so weak. These measurements were discarded. There were a few spectra in which the measured fluxes deviated strongly from more plausible values obtained from redundant spectra obtained at the same epoch (i.e., during the same 8-hour observing shift). We are not always able to identify specific causes of these deviant points; some effects, such as grazing-incidence cosmic rays, are notoriously difficult to remove from *IUE* spectra through the standard pipeline processing methods such as NEWSIPS. We elected to simply remove the strongly deviant values from the light curves before processing. The measurements of the continuum and emission-line fluxes used in this analysis are given in Tables 2–5.

Multiple measurements that were obtained within a single 8-hour *IUE* observing shift were compared to determine uncertainties in the fluxes on the assumption that no real detectable variability occurred on such short time scales. Following this, data points obtained in a single shift were replaced by a weighted average to form the final light curves shown in the left-hand columns of Figs. 1–2 and which were used as the basis for the time-series analysis described in §3.1. The statistical properties of these light curves are summarized in Table 6. Column (1) identifies the spectral feature and column (2) gives the total number of measurements in the time series. The average and median intervals between individual data points are given in columns (3) and (4), respectively. The mean flux and its standard deviation appear in column (5). The mean fractional error, based on comparison of closely spaced observations, is given in column (6). Column (7) gives the “excess variance” for each light curve, computed as

$$F_{\text{var}} = \frac{\sqrt{\sigma^2 - \delta^2}}{\langle f \rangle}, \quad (2)$$

where σ^2 is the variance of all of the fluxes, δ^2 is the mean square uncertainty of the fluxes and $\langle f \rangle$ is the mean flux for all observations. Also listed in column (8) is R_{max} , the ratio of

the maximum and minimum fluxes for each time series.

3. DATA ANALYSIS

3.1. Time Series Analysis

To find the time delay between the continuum and emission-line variations, we cross-correlate each of the emission-line light curves with that of the 1355 Å continuum. The methodology we employ is the interpolation correlation function method as described by White & Peterson (1994). The cross-correlation functions (CCFs) for the emission lines are shown in the right-hand columns of Figs. 1 and 2. In order to assess uncertainties in the time-delay measurements, we employ the model-independent Monte Carlo FR/RSS method described by Peterson et al. (1998), with some modifications introduced by Peterson et al. (2004), which works as follows. For a single realization, a light curve of N data points is sampled N times without regard to whether or not any given point has been previously selected; this is called “random subset sampling,” or RSS. Any data point that is selected M times has its uncertainty in flux reduced by a factor $M^{1/2}$. The fluxes in each of the selected N points are altered by random Gaussian deviates based on their adopted error bars; we refer to this as “flux randomization,” or FR. The subset of these points, sampled and altered by the FR/RSS algorithm, are then cross-correlated as though they were real data. This yields a CCF like those seen in Figs. 1 and 2. We locate the peak value r_{\max} of the CCF, which occurs at a time lag τ_{peak} . We also compute the centroid of the CCF, τ_{cent} , based on those points near the peak with values $r \gtrsim 0.8r_{\max}$. A large number of such Monte Carlo realizations builds up a cross-correlation peak distribution (CCPD) for τ_{peak} and a cross-correlation centroid distribution (CCCD) for τ_{cent} . As argued elsewhere, τ_{cent} is more repeatable and has a clearer physical interpretation, so we prefer it to τ_{peak} . We thus take the average values of the CCCD and CCPD to be τ_{cent} and τ_{peak} , respectively. The uncertainties $\Delta\tau_{\text{upper}}$ and $\Delta\tau_{\text{lower}}$ are computed such that 15.87% of the CCCD realizations have values $\tau < \tau_{\text{cent}} - \Delta\tau_{\text{lower}}$ and 15.87% of the CCCD realizations have values $\tau > \tau_{\text{cent}} + \Delta\tau_{\text{upper}}$, with the errors in τ_{peak} defined similarly. These uncertainties correspond to $\pm 1\sigma$ for a Gaussian distribution. The values so computed for these data sets are given in Table 7. Note that the errors are generally asymmetric, but usually not strongly so. It should be noted that formally these observed-frame measurements need to be corrected for time dilation by division by $(1+z)$, where the systemic redshift of NGC 4151 is $z = 0.00332$.

3.2. Line Width Measurement

To obtain the black hole mass, we also need to measure the width of each emission line. Indeed, we wish to measure the line-of-sight velocity distribution for the *variable* part of the emission-line, specifically avoiding contaminating non-variable (on reverberation timescales) components, such as a contribution from the much larger narrow-line region. We use all of the spectra obtained during the observing campaign to construct a mean spectrum and a root-mean-square (rms) spectrum; the rms spectrum isolates the variable part of the emission lines. In Figs. 3 and 4, we show the mean and rms spectra for the SWP and LWP images from 1988 and 1991, respectively.

To measure the emission-line widths, we first interpolate the rms continuum under the emission lines by fitting a linear continuum in the continuum windows given in Table 1. We then characterize the line width in two ways, by its full-width at half maximum (FWHM) and by the second moment of the line profile, i.e., the line dispersion σ_{line} , as described by Peterson et al. (2004). To evaluate the uncertainties in these measurements, we follow the procedure described by Peterson et al. (2004), using a procedure similar in spirit to that used to evaluate uncertainties in the time delays. For a sample of N spectra, we select N spectra at random, in each case without regard to whether or not a particular spectrum has been previously selected. These N random spectra are used to construct mean and rms spectra, and both line width measurements are made for each emission line. This constitutes one Monte Carlo realization. A large number of similar realizations yields a mean and standard deviation for each line-width measure. Line width measurements and associated uncertainties for each of the emission lines are given in Table 8. The emission-line widths here have been converted to the rest-frame of NGC 4151 and have been adjusted as described by Peterson et al. (2004) to account for the resolution of the *IUE* spectrograph. We note that we prefer σ_{line} over FWHM as a line width measure for a variety of reasons, including that it is generally more repeatable in noisy spectra (which rms spectra often are).

Two obvious difficulties are apparent upon inspection of Figs. 3 and 4. The first of these is that the core of the C IV emission line is strongly self-absorbed. This is very apparent in the rms spectra, and is especially strong in the 1991 data. It is impossible to correct for this absorption since we do not know the intrinsic unabsorbed C IV profile. However, we can try to assess the severity of the systematic uncertainty by modeling the intrinsic profile in a variety of ways to see how much the line width measurement might change. We experimented with various means of accounting for the effects of the absorption, and the largest change in line width was obtained by fitting the unabsorbed wings of the emission line with a Gaussian. The Gaussian so constructed had a value of σ_{line} that was about 10% smaller than that obtained in our direct measurement, and the value of FWHM, which

is more sensitive to the flux at line center, decreased by more than 20%. We can regard our measurement of the C IV line width as an upper limit that is probably not a terrible overestimate of the true unabsorbed value of σ_{line} . In any case, the effect on the black hole mass estimate is quite insignificant given the level of accuracy that we can currently achieve in black hole mass measurement. We also note that the Mg II line is self-absorbed, but the absorption is much weaker and the emission line in the rms spectrum is too noisy for the absorption feature to be apparent.

A second difficulty is that the C IV and He II emission lines are strongly blended in their wings. Since these cannot be uniquely deblended, we make the approximation that the both lines are approximately symmetric about line center and use the unblended half of each line (the short wavelength side for C IV and the long wavelength side for He II) to determine the width. These are the values of the line widths that appear in Table 8.

4. THE BLACK HOLE MASS

As noted earlier and as observed in other sources, we expect that if the dynamics of the BLR are dominated by the gravitational force of the central black hole, we should see a virial relationship between emission-line widths and time lags of the form $\Delta V \propto \tau^{-1/2}$. To test this for NGC 4151, we plot the emission-line line widths from the rms spectra (Table 8) versus the measured time delays (Table 7) in Fig. 5. We supplement the UV data with measurements of the H α and H β line widths and lags from Peterson et al. (2004), based on data originally published by Maoz et al. (1991) and Kaspi et al. (1996). There is considerable scatter in Fig. 5, but with the exception of the H α and H β measurements based on the Kaspi et al. (1996) monitoring program, the scatter is similar to that seen in other sources (cf. Peterson et al. 2004). The range of lags in this diagram is less than a factor of 3, whereas in the similar plot for NGC 5548 (cf. Fig. 3 of Peterson et al. 2004), the range of lags is nearly a factor of 15. Moreover, given the limited quality of the monitoring data on NGC 4151, it is perhaps surprising that the results are as good as they appear to be. Neither of the two UV monitoring data sets on NGC 4151 are remarkably good: the 1988 *IUE* data are slightly undersampled and the duration of the 1991 experiment was somewhat short, especially in the case of the Mg II observations, the effect of which is apparent in its flat-topped CCF (Fig. 2). The only UV line not affected by self-absorption or blending is C III], for which the variations are comparatively weak.

The two existing optical data sets are even more problematic. In the case of the 1988 data from Maoz et al. (1991), the emission-line lags appear to be well determined, but it is difficult to measure reliably the width of the broad-line component in these spectra.

In NGC 4151, the narrow-line components are much stronger relative to the broad-line components than they are in most type 1 AGNs. The spectra from this campaign are rather low resolution, so the [O III] lines are partially blended with one another. Moreover, the line-spread function appears to vary among the spectra, possibly as a result of drift in the large aperture that was used to ensure an accurate flux calibration. The combination of these factors makes it hard to isolate the broad-line component and determine their widths with great confidence. Nevertheless, the $H\alpha$ and $H\beta$ lags and line widths as plotted in Fig. 5 are reasonably consistent with the virial relationship derived from the UV lines in this object.

On the other hand, the optical data described by Kaspi et al. (1996) present some serious difficulties for a virial interpretation. However, in this particular case, the nature of the variations during this campaign were not favorable for reverberation analysis — both the continuum and emission lines showed nearly monotonically increasing flux throughout the monitoring period, and the amplitude of variation was relatively low. Without a strong change in the sign of the first derivative of the light curves, as seen in the light curves in Figs. 1 and 2, it is difficult to obtain a highly reliable reverberation lag. In an attempt to mitigate the unfavorable effects of a monotonic rise, we experimented with removing the long-term trend in these data prior to cross-correlating the time series (i.e., “detrending” the data, cf. Welsh 1999), and this had the effect of moving the already-small lag even closer to zero. Our suspicion is that this lag measurement is spurious. It seems likely that at such a low level of variability, there are correlated errors between the continuum and emission-line measurements, which manifest themselves as a correlated signal at zero lag. We have not been able to demonstrate this conclusively and thus need to keep in mind the possibility that these measurements represent an actual deviation from the virial relationship. However, given the unfavorable nature of the observed variations, we are more inclined at the present time to simply disregard this particular data set.

The best-fit slope to all of the data points in Fig. 5 is -1.52 ± 0.84 , which differs from the virial slope of -0.5 by only 1.2σ . Obviously additional, better data will be required to determine whether or not the virial relationship between lag and line widths holds in the case of NGC 4151.

Setting aside this difficulty, we nevertheless proceed with an estimate of the mass of the central black hole by using eq. (1) with the scaling factor $f = 5.5$, as determined by Onken et al. (2004) by normalizing the AGN $M_{\text{BH}}-\sigma_*$ to that for quiescent galaxies. We use τ_{cent} for the time delay and σ_{line} to characterize the line width. If we use all of the data in Fig. 5, we find a black hole mass $M_{\text{BH}} = (2.58 \pm 0.35) \times 10^7 M_{\odot}$, based on a weighted average of the individual mass estimates for each line. If we restrict the mass estimate to the UV data

points from the present work, we obtain a mass estimate of $M_{\text{BH}} = (8.55 \pm 1.26) \times 10^7 M_{\odot}$. Our preferred estimate is obtained by eliminating the most problematic data, leaving only C III], He II, and Mg II from the two UV campaigns. The resulting mass estimate is $M_{\text{BH}} = (4.14 \pm 0.73) \times 10^7 M_{\odot}$. We remind the reader, however, that due to unquantified systematic uncertainties (as embodied in the scale factor f in eq. 1), this is probably uncertain by a factor of 3–4 (Onken et al. 2004), as are all reverberation-based mass estimates.

5. CONCLUSIONS

In this contribution, we have examined archival *IUE* spectra that have been reprocessed with the NEWSIPS software. For two separate monitoring programs, we were able to obtain emission-line time delays for C IV $\lambda 1549$, He II $\lambda 1640$, C III] $\lambda 1909$, and Mg II $\lambda 2798$. Unfortunately, the lags span a very narrow range, even when optical Balmer line measurements from ground-based campaigns are included, precluding a strong test of the expected virial relationship, $\Delta V \propto \tau^{-1/2}$. Clearly additional data are required to clarify the situation.

Ignoring this difficulty for the time being, we obtain an estimate of the mass of the central black hole by combining our time delay measurements with line-width measurements. Based on the subset of lines that we regard as most reliable, we provide an estimate of the black hole mass of $M_{\text{BH}} = (4.14 \pm 0.73) \times 10^7 M_{\odot}$. This is a factor of ~ 3 higher than the previous estimate of $M_{\text{BH}} = (1.33 \pm 0.46) \times 10^7 M_{\odot}$ from Peterson et al. (2004); the earlier estimate was based on the optical data from Kaspi et al. (1996), which are somewhat problematic. Indeed, problems with the existing optical data have led us to carry out a new optical reverberation program, the results of which will be reported elsewhere (Bentz et al. 2006b).

It is also worth noting that the higher mass estimate means that the black hole radius of influence, $r = GM_{\text{BH}}/\sigma_*^2 \approx 19$ pc, is larger than previously supposed, projecting to an angular radius of $0''.28$. This makes NGC 4151 one of the best candidates for black hole measurement by other direct means that depend on high angular resolution.

We are grateful for support of this program by the NSF through grant AST-0205964 and by NASA through grant HST GO-09849 from the Space Telescope Science Institute.

REFERENCES

- Bentz, M.C., Peterson, B.M., Pogge, R.W., Vestergaard, M., & Onken, C.A. 2006a, ApJ, in press
- Bentz, M.C., et al. 2006b, submitted to ApJ
- Blandford, R.D., & McKee, C.F. 1982, ApJ, 255, 419
- Cackett, E.M., & Horne, K. 2006, MNRAS, 365, 1180
- Clavel, J., Boksenberg, A., Bromage, G.E., Elvius, A., Penston, M.V., Perola, G.C., Santos-Lleó, M., Snijders, M.A.J. & Ulrich, M.-H. 1990, MNRAS, 246, 668
- Crenshaw, D.M., et al. 1996, ApJ, 470, 322
- Ferrarese, L., & Merritt, D. 2000, ApJ, 539, L9
- Ferrarese, L., Pogge, R.W., Peterson, B.M., Merritt, D., Wandel, A., & Joseph, C.L. 2001, ApJ, 555, L79
- Gebhardt, K., et al. 2000a, ApJ, 539, L13
- Gebhardt, K., et al. 2000b, ApJ, 543, L5
- Kaspi, S., Maoz, D., Netzer, H., Peterson, B.M., Vestergaard, M, & Jannuzi, B.T. 2005, ApJ, 629, 61
- Kaspi, S., Smith, P.S., Netzer, H., Maoz, D., Jannuzi, B.T., & Giveon, U. 2000, ApJ, 533, 631
- Kaspi, S., et al. 1996, ApJ, 470, 336
- Kollatschny, W. 2003, A&A, 407, 461
- Kollmeier, J.A., Onken, C.A., Kochanek, C.S., Gould, A., Weinberg, D.H., Dietrich, M., Cool, R., Dey, A., Eisenstein, D.J., Jannuzi, B.T., Le Floch, E., & Stern, D. 2006, submitted to ApJ, (astro-ph/0508657)
- Maoz, D., Netzer, H., Mazeh, T., Beck, S., Almoznino, E., Leibowitz, E., Brosch, N., Mendelson, H. & Laor, A. 1991, ApJ, 367, 493
- McLure, R.J., & Jarvis, M.J. MNRAS, 337, 109
- Nelson, C.H., Green, R.F., Bower, G., Gebhardt, K., & Weistrop, D. 2004, ApJ, 615, 652

- Onken, C.A., Ferrarese, L., Merritt, D., Peterson, B.M., Pogge, R.W., Vestergaard, M., & Wandel, A. 2004, *ApJ*, 615, 645
- Onken, C.A., & Peterson, B.M. 2002, *ApJ*, 572, 746
- Onken, C.A., Peterson, B.M., Dietrich, M., Robinson, A., & Salamanca, I.M. 2003, *ApJ*, 585, 121
- Peterson, B.M. 1993, *PASP*, 105, 247
- Peterson, B.M., & Wandel, A 1999, *ApJ*, 521, L95
- Peterson, B.M., & Wandel, A 2000, *ApJ*, 540, L13
- Peterson, B.M., et al. 2004, *ApJ*, 613, 682
- Peterson, B.M., Wanders, I., Horne, K., Collier, S., Alexander, T., & Kaspi, S. 1998, *PASP*, 110, 660
- Tremaine, S., et al. 2002, *ApJ*, 574, 740
- Ulrich, M.-H. & Horne, K. 1996, *MNRAS*, 283, 748
- Vestergaard, M. 2002, *ApJ*, 571, 733
- Vestergaard, M. 2004, *ApJ*, 601, 676
- Vestergaard, M., & Peterson, B.M. 2006, *ApJ*, 641, 689
- Wandel, A., Peterson, B.M., & Malkan, M.A., 1999, *ApJ*, 526, 579
- Welsh, W.F. 1999, *PASP*, 111, 1347
- White, R.J. & Peterson, B.M. 1994, *PASP*, 106, 879

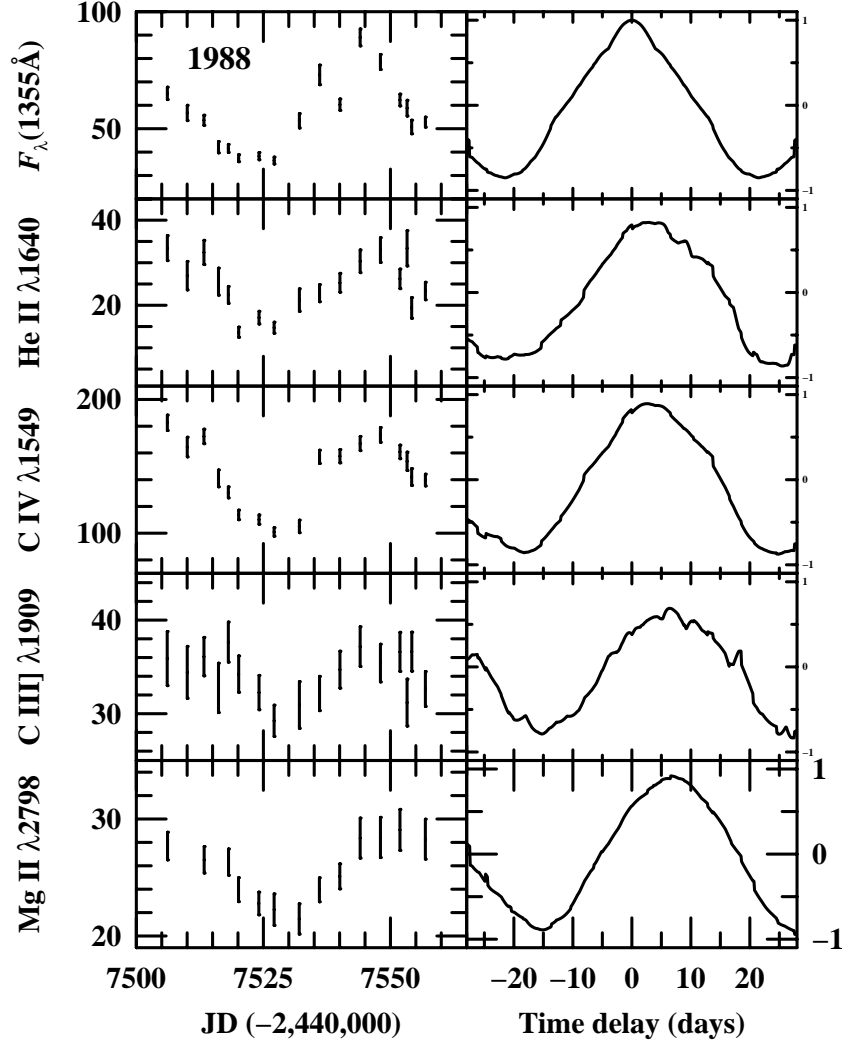


Fig. 1.— Light curves and cross-correlation functions based on the 1988 *IUE* observations of NGC 4151. The left column shows flux as a function of Julian date, from top to bottom, for the continuum flux at 1355 Å, and the emission-line fluxes for He II λ 1640, C IV λ 1549, C III] λ 1909, and Mg II λ 2798, as listed in Tables 2 and 3. The continuum flux is plotted in units of 10^{-15} ergs s $^{-1}$ cm $^{-2}$ Å $^{-1}$ and the emission-line fluxes are in units of 10^{-13} ergs s $^{-1}$ cm $^{-2}$. The right column shows the result of cross-correlating each of these light curves with the 1355 Å continuum light curve; the top panel is thus the continuum autocorrelation function.

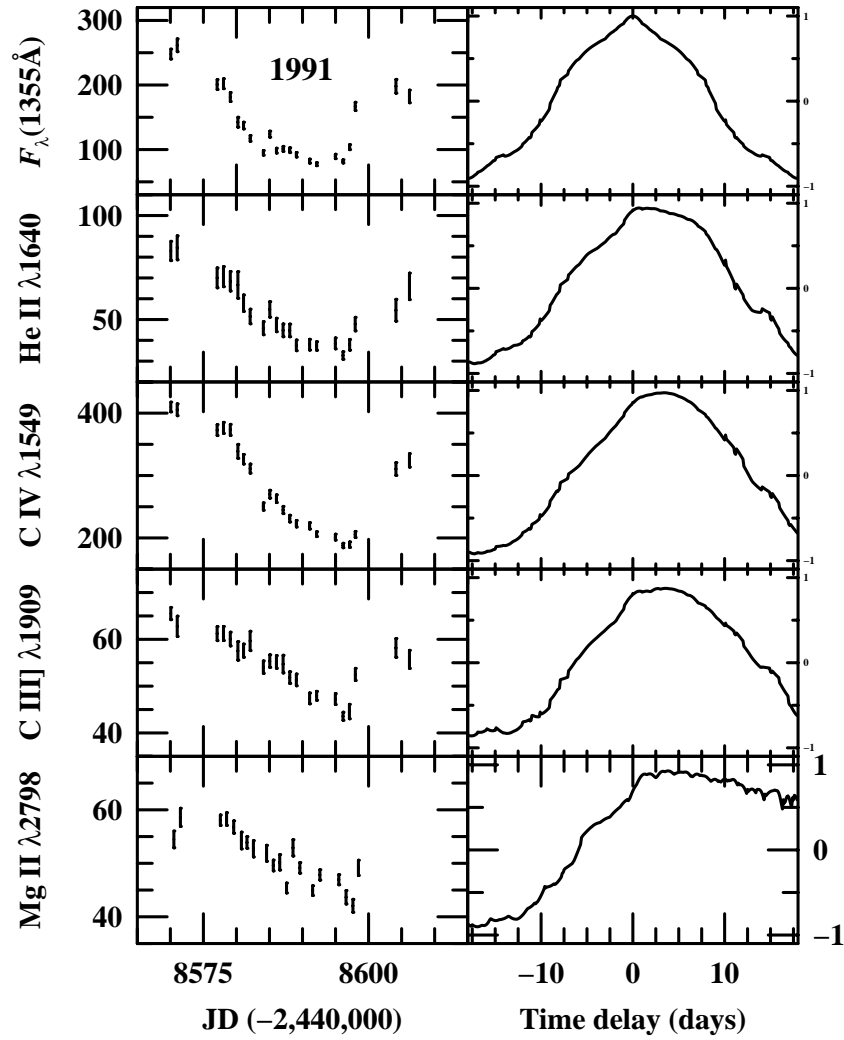


Fig. 2.— Light curves and cross-correlation functions based on the 1991 *IUE* observations of NGC 4151, as listed in Tables 4 and 5, and plotted as in Fig. 1.

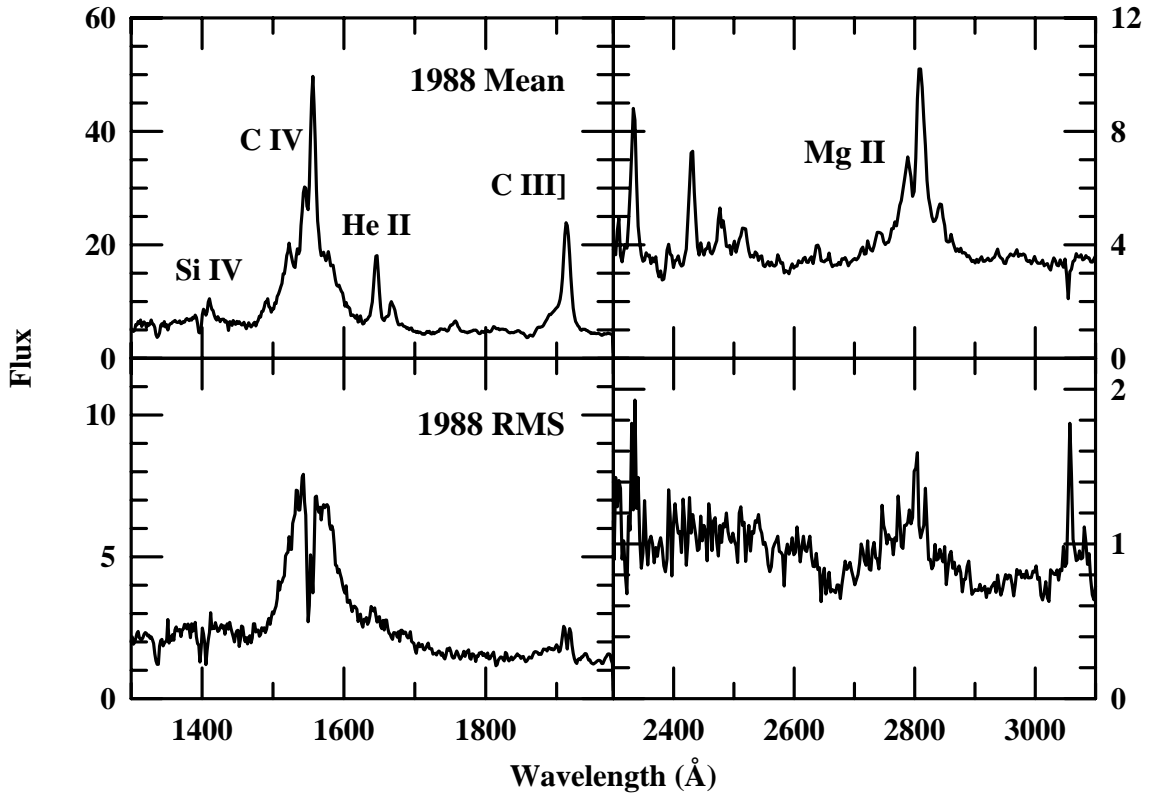


Fig. 3.— Mean and rms spectra based on the 1988 *IUE* observations of NGC 4151. The left column shows the mean (upper panel) and rms (lower panel) spectra formed from the SWP data. The right column shows the mean (upper panel) and rms (lower panel) spectra formed from the LWP data. Fluxes are in units of 10^{-15} ergs s $^{-1}$ cm $^{-2}$ Å $^{-1}$ and the spectra are plotted in the observed frame.

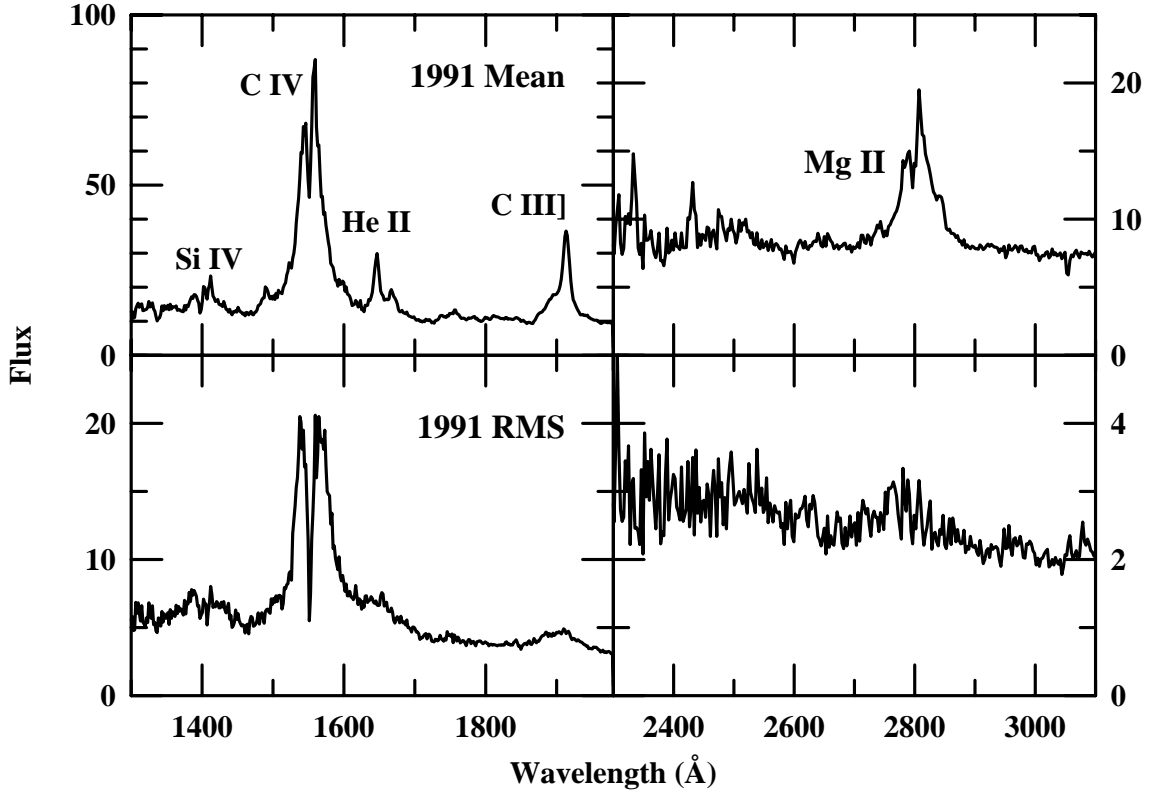


Fig. 4.— Mean and rms spectra based on the 1991 *IUE* observations of NGC 4151. The left column shows the mean (upper panel) and rms (lower panel) spectra formed from the SWP data. The right column shows the mean (upper panel) and rms (lower panel) spectra formed from the LWP data. Fluxes are in units of $10^{-15} \text{ ergs s}^{-1} \text{ cm}^{-2} \text{ \AA}^{-1}$ and the spectra are plotted in the observed frame.

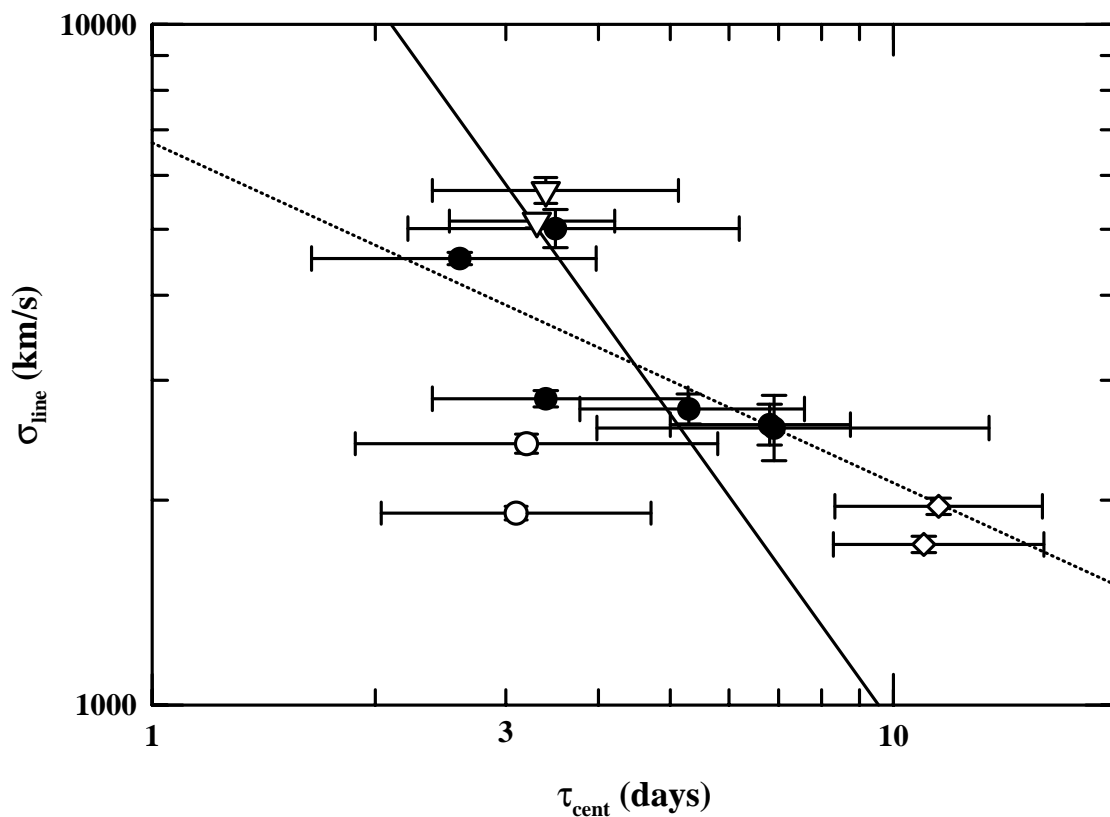


Fig. 5.— Emission-line widths (as characterized by line dispersion), versus time lags for lines in NGC 4151. The closed circles are the UV emission lines listed in Tables 7 and 8, except for the C IV lines, which are shown as inverted open triangles. The open circles and diamonds are hydrogen Balmer-line measurements from 1987 and 1993, respectively, as analyzed by Peterson et al. (2004). The solid line has a slope of -1.52 ± 0.84 and is the best fit to all the data, and the dotted line is the best fit for a forced slope of $-1/2$, i.e., a virial relationship. The filled symbols represent the more trustworthy measurements.

Table 1. Line Integration Limits

Emission Line	Line Integration Limits (Å)	Continuum Window (Å)	Continuum Window (Å)
1988 C IV λ 1549	1470–1620	1440–1470	1700–1730
1988 He II λ 1640	1620–1700	1465–1475	1730–1740
1988 C III] λ 1909	1863–1937	1845–1855	1965–1975
1988 Mg II λ 2798	2750–2853	2600–2620	2890–2900
1991 C IV λ 1549	1475–1602	1465–1475	1700–1705
1991 He II λ 1640	1602–1700	1465–1475	1730–1740
1991 C III] λ 1909	1863–1937	1845–1855	1965–1975
1991 Mg II λ 2798	2750–2853	2600–2620	2890–2900

Table 2. 1988 SWP Flux Measurements

Image Name	Julian Date –2, 440, 000	$F_{\lambda}(1355 \text{ \AA})^1$	C IV $\lambda 1549^2$	He II $\lambda 1640^2$	C III] $\lambda 1909^2$
SWP34845	7497.992	...	227.48 ± 10.20	53.17 ± 6.62	34.56 ± 2.78
SWP34868	7499.549	93.96 ± 5.42	229.65 ± 10.29	52.57 ± 6.54	35.83 ± 2.89
SWP34869	7499.630	98.90 ± 5.71	...	52.22 ± 6.50	...
SWP34998	7506.075	66.55 ± 3.84	184.00 ± 8.25	33.00 ± 4.11	35.89 ± 2.89
SWP34999	7506.132	63.77 ± 3.68	181.19 ± 8.12	33.89 ± 4.22	...
SWP35028	7510.017	56.74 ± 3.27	164.41 ± 7.37	26.95 ± 3.35	34.42 ± 2.77
SWP35058	7513.273	55.10 ± 3.18	177.79 ± 7.97	31.98 ± 3.98	37.16 ± 2.99
SWP35059	7513.335	52.24 ± 3.01	167.54 ± 7.51	32.88 ± 4.09	35.14 ± 2.83
SWP35090	7516.165	42.08 ± 2.43	140.97 ± 6.32	25.55 ± 3.18	32.76 ± 2.64
SWP35098	7518.066	39.73 ± 2.92	131.98 ± 5.92	24.39 ± 3.04	37.02 ± 2.98
SWP35099	7518.135	43.86 ± 2.53	129.10 ± 5.79	20.99 ± 2.61	38.33 ± 3.09
SWP35123	7520.111	37.91 ± 2.19	107.59 ± 4.82	12.30 ± 1.53	33.28 ± 2.68
SWP35124	7520.166	36.93 ± 2.13	121.40 ± 5.44	15.95 ± 1.99	35.30 ± 2.84
SWP35171	7524.109	38.22 ± 2.21	114.64 ± 5.14	17.60 ± 2.19	32.87 ± 2.65
SWP35172	7524.171	38.29 ± 2.21	106.29 ± 4.76	16.64 ± 2.07	31.69 ± 2.55
SWP35210	7527.075	33.30 ± 1.92	100.50 ± 4.51	13.06 ± 1.63	27.38 ± 2.21
SWP35211	7527.143	41.09 ± 2.37	101.39 ± 4.55	17.84 ± 2.22	31.76 ± 2.56
SWP35264	7532.083	53.37 ± 3.08	105.06 ± 4.71	21.22 ± 2.64	30.93 ± 2.49
SWP35297	7536.019	...	153.93 ± 6.90	21.15 ± 2.63	31.92 ± 2.57
SWP35298	7536.075	72.98 ± 4.21	160.55 ± 7.20	25.25 ± 3.14	32.40 ± 2.61
SWP35330	7540.032	58.89 ± 3.40	160.04 ± 7.17	25.96 ± 3.23	36.94 ± 2.98
SWP35331	7540.091	61.76 ± 3.56	155.24 ± 6.56	24.67 ± 3.07	32.93 ± 2.65
SWP35374	7544.004	86.76 ± 5.00	163.48 ± 7.33	28.77 ± 3.58	39.64 ± 3.19
SWP35375	7544.070	91.49 ± 5.28	170.93 ± 7.66	32.32 ± 4.02	35.22 ± 2.84
SWP35388	7547.998	79.78 ± 4.60	175.48 ± 7.87	33.62 ± 4.18	34.70 ± 2.80
SWP35389	7548.059	77.33 ± 4.46	171.56 ± 7.69	32.38 ± 4.03	36.17 ± 2.91
SWP35403	7551.842	65.30 ± 3.77	172.33 ± 7.72	24.95 ± 3.11	39.66 ± 3.20
SWP35404	7551.901	59.71 ± 3.44	151.81 ± 6.81	27.76 ± 3.45	34.32 ± 2.77
SWP35417	7553.270	58.73 ± 3.39	153.76 ± 6.89	32.38 ± 4.15	31.19 ± 2.51
SWP35428	7554.177	50.73 ± 2.93	142.02 ± 6.37	19.38 ± 2.45	37.88 ± 3.05

Table 2—Continued

Image Name	Julian Date –2,440,000	$F_{\lambda}(1355 \text{ \AA})^1$	C IV $\lambda 1549^2$	He II $\lambda 1640^2$	C III] $\lambda 1909^2$
SWP35429	7554.232	35.53 ± 2.86
SWP35457	7556.842	51.04 ± 2.94	139.96 ± 6.27	21.38 ± 2.66	31.65 ± 2.55
SWP35458	7556.908	54.85 ± 3.16	139.51 ± 6.25	26.34 ± 3.28	33.77 ± 2.72

¹Continuum fluxes are in units of $10^{-15} \text{ erg cm}^2 \text{ s}^{-1} \text{ \AA}^{-1}$

²Emission-line fluxes are in units of $10^{-13} \text{ erg cm}^{-2} \text{ s}^{-1}$

Table 3. 1988 Mg II λ 2798 Flux Measurements

Image Name	Julian Date ($-2, 440, 000$)	Mg II λ 2798 ¹
LWP00505	7499.610	28.31 ± 1.71
LWP00506	7499.680	29.35 ± 1.77
LWP14603	7506.100	26.01 ± 1.57
LWP14604	7506.180	29.91 ± 1.81
LWP14660	7513.310	25.84 ± 1.56
LWP14661	7513.380	27.25 ± 1.65
LWP14694	7518.100	26.38 ± 1.60
LWP14695	7518.180	26.26 ± 1.59
LWP14704	7520.070	25.26 ± 1.53
LWP14705	7520.140	22.90 ± 1.38
LWP14730	7524.070	22.92 ± 1.39
LWP14731	7524.140	22.64 ± 1.37
LWP14748	7527.110	22.25 ± 1.35
LWP14773	7532.050	21.46 ± 1.30
LWP14794	7535.990	22.51 ± 1.36
LWP14795	7536.050	25.84 ± 1.56
LWP14814	7540.000	25.88 ± 1.56
LWP14815	7540.070	24.40 ± 1.48
LWP14855	7544.040	28.37 ± 1.72
LWP14888	7548.030	28.42 ± 1.72
LWP14917	7551.870	29.07 ± 1.76
LWP14941	7556.870	28.28 ± 1.71

¹Emission-line fluxes are in units of 10^{-13}
erg cm⁻² s⁻¹

Table 4. 1991 SWP Flux Measurements

Image Name	Julian Date (−2, 440, 000)	$F_{\lambda}(1355 \text{ \AA})^1$	C IV $\lambda 1549^2$	He II $\lambda 1640^2$	C III] $\lambda 1909^2$
SWP43044	8570.007	245.39 ± 5.77	406.54 ± 13.49	82.65 ± 7.99	64.11 ± 2.22
SWP43045	8570.063	239.55 ± 5.64	403.02 ± 13.37	76.72 ± 7.41	67.28 ± 2.33
SWP43046	8570.112	260.85 ± 6.14	420.93 ± 13.97	92.43 ± 8.93	65.30 ± 3.36
SWP43052	8571.005	254.54 ± 5.99	412.64 ± 13.69	83.22 ± 8.04	62.78 ± 2.17
SWP43053	8571.066	269.34 ± 6.34	398.57 ± 13.22	85.81 ± 8.29	...
SWP43117	8577.048	203.85 ± 4.80	367.67 ± 12.20	65.38 ± 6.32	62.16 ± 2.15
SWP43118	8577.106	197.79 ± 4.65	378.25 ± 12.55	76.38 ± 7.38	60.35 ± 2.09
SWP43129	8578.010	204.50 ± 4.81	377.99 ± 12.54	71.34 ± 6.89	60.88 ± 2.11
SWP43130	8578.070	199.65 ± 4.70	374.75 ± 12.43	69.92 ± 6.76	61.63 ± 2.13
SWP43142	8579.039	184.62 ± 4.34	380.52 ± 12.62	64.63 ± 6.24	61.61 ± 2.13
SWP43143	8579.097	178.35 ± 4.20	366.47 ± 12.16	73.22 ± 7.07	58.66 ± 2.03
SWP43155	8580.221	142.40 ± 3.35	338.72 ± 11.24	66.61 ± 6.44	57.54 ± 1.99
SWP43162	8581.042	135.03 ± 3.18	312.80 ± 10.38	59.22 ± 5.72	58.29 ± 2.02
SWP43163	8581.104	139.46 ± 3.28	342.05 ± 11.35	56.62 ± 5.47	56.91 ± 1.97
SWP43172	8582.041	118.19 ± 2.78	309.46 ± 10.27	52.90 ± 5.11	59.66 ± 2.07
SWP43173	8582.105	116.39 ± 2.74	312.81 ± 10.38	50.19 ± 4.85	...
SWP43190	8584.037	94.71 ± 2.23	241.56 ± 8.01	43.53 ± 4.21	54.78 ± 1.90
SWP43191	8584.107	95.05 ± 2.24	260.56 ± 8.64	48.69 ± 4.70	53.40 ± 1.85
SWP43209	8585.011	125.42 ± 2.95	268.44 ± 8.91	53.17 ± 5.14	54.27 ± 1.88
SWP43210	8585.085	122.28 ± 2.88	271.76 ± 9.02	56.85 ± 5.49	56.52 ± 1.96
SWP43218	8586.016	101.55 ± 2.39	255.73 ± 8.48	49.47 ± 4.78	53.54 ± 1.85
SWP43219	8586.092	95.54 ± 2.25	270.95 ± 8.90	45.61 ± 4.41	57.01 ± 1.97
SWP43228	8587.026	99.96 ± 2.35	232.37 ± 7.71	40.45 ± 3.91	54.71 ± 1.89
SWP43229	8587.093	102.14 ± 2.40	260.29 ± 8.64	51.99 ± 5.02	...
SWP43234	8588.036	101.84 ± 2.40	230.84 ± 7.66	44.33 ± 4.28	50.15 ± 1.74
SWP43235	8588.107	96.60 ± 2.27	231.07 ± 7.67	45.21 ± 4.37	53.76 ± 1.86
SWP43244	8589.028	90.57 ± 2.13	223.64 ± 7.42	39.69 ± 3.83	51.81 ± 1.79
SWP43245	8589.105	93.37 ± 2.20	221.94 ± 7.36	35.87 ± 3.47	50.87 ± 1.76
SWP43275	8591.043	81.99 ± 1.93	215.17 ± 7.14	36.80 ± 3.56	49.47 ± 1.71
SWP43276	8591.170	82.17 ± 1.93	224.04 ± 7.43	39.18 ± 3.79	45.60 ± 1.58

Table 4—Continued

Image Name	Julian Date (−2, 440, 000)	$F_{\lambda}(1355 \text{ \AA})^1$	C IV $\lambda 1549^2$	He II $\lambda 1640^2$	C III] $\lambda 1909^2$
SWP43285	8592.070	80.64 ± 1.90	200.22 ± 6.64	36.53 ± 3.53	47.20 ± 1.63
SWP43286	8592.172	79.79 ± 1.88	215.40 ± 7.15	37.15 ± 3.59	49.36 ± 1.71
SWP43287	8592.192	72.84 ± 1.71	203.96 ± 6.77	38.32 ± 3.70	47.34 ± 1.64
SWP43314	8594.934	89.00 ± 2.09	197.04 ± 6.54	37.70 ± 3.64	47.48 ± 1.64
SWP43315	8595.006	89.68 ± 9.90	205.95 ± 6.83	39.44 ± 3.81	47.00 ± 1.63
SWP43323	8596.061	83.24 ± 1.96	174.03 ± 5.77	34.55 ± 3.34	43.31 ± 1.50
SWP43324	8596.138	82.76 ± 1.95	193.47 ± 6.42	35.98 ± 3.48	46.14 ± 1.60
SWP43325	8596.191	79.34 ± 1.87	200.13 ± 6.64	29.23 ± 2.82	41.69 ± 1.44
SWP43333	8597.099	102.94 ± 2.42	182.50 ± 6.06	36.23 ± 3.50	44.57 ± 1.54
SWP43334	8597.170	104.69 ± 2.46	196.99 ± 6.54	39.83 ± 3.85	...
SWP43340	8597.936	164.78 ± 3.88	201.26 ± 6.68	47.49 ± 4.59	51.18 ± 1.77
SWP43341	8598.014	169.04 ± 3.98	210.27 ± 6.97	48.12 ± 4.65	53.99 ± 1.87
SWP43373	8604.141	198.04 ± 4.66	310.46 ± 10.30	54.47 ± 5.26	58.17 ± 2.01
SWP43392	8606.188	182.24 ± 4.29	324.30 ± 10.76	65.95 ± 6.37	55.72 ± 1.93

¹Continuum values are in units of $10^{-15} \text{ erg cm}^{-2} \text{ s}^{-1} \text{ \AA}^{-1}$.

²Emission line fluxes are in units of $10^{-13} \text{ erg cm}^{-2} \text{ s}^{-1}$.

Table 5. 1991 Mg II λ 2798 Flux Measurements

Image Name	Julian Date ($-2, 440, 000$)	Mg II λ 2798 ¹
LWP21671	8570.530	54.45 \pm 1.56
LWP21681	8571.520	58.60 \pm 1.70
LWP21750	8577.500	57.02 \pm 1.65
LWP21751	8577.570	56.87 \pm 1.64
LWP21752	8577.620	60.61 \pm 1.75
LWP21764	8578.480	58.65 \pm 1.70
LWP21765	8578.530	57.92 \pm 1.68
LWP21774	8579.560	56.47 \pm 1.63
LWP21775	8579.610	57.10 \pm 1.65
LWP21785	8580.750	54.26 \pm 1.57
LWP21791	8581.570	54.56 \pm 1.58
LWP21792	8581.620	53.27 \pm 1.54
LWP21798	8582.570	52.71 \pm 1.52
LWP21827	8584.560	51.87 \pm 1.50
LWP21835	8585.540	48.67 \pm 1.41
LWP21836	8585.610	50.59 \pm 1.46
LWP21845	8586.550	50.20 \pm 1.45
LWP21854	8587.550	45.81 \pm 1.33
LWP21855	8587.610	44.98 \pm 1.30
LWP21863	8588.560	52.89 \pm 1.53
LWP21872	8589.560	49.81 \pm 1.44
LWP21873	8589.630	48.52 \pm 1.40
LWP21893	8591.460	46.38 \pm 1.34
LWP21894	8591.570	43.59 \pm 1.26
LWP21904	8592.600	46.45 \pm 1.34
LWP21905	8592.660	49.40 \pm 1.43
LWP21930	8595.460	47.18 \pm 1.36
LWP21931	8595.530	46.71 \pm 1.35
LWP21943	8596.590	43.65 \pm 1.26
LWP21956	8597.630	42.06 \pm 1.22

Table 5—Continued

Image Name	Julian Date (−2, 440, 000)	Mg II λ 2798 ¹
LWP21965	8598.460	49.16 ± 1.42

¹Emission-line fluxes are in units of 10^{-13}
erg cm^{−2} s^{−1}

Table 6. Light Curve Statistics

Time Series (1)	<i>N</i> (2)	Sampling Interval (days)		Mean Flux ¹ (5)	Mean Fractional Error (6)	<i>F</i> _{var} (7)	<i>R</i> _{max} (8)
		$\langle T \rangle$ (3)	<i>T</i> _{median} (4)				
1988 1355 Å	18	3.4	3.8	58.1 ± 17.3	0.046	0.293	2.65 ± 0.15
1988 C IV	19	3.3	3.6	154.2 ± 35.6	0.036	0.228	2.28 ± 0.13
1988 He II	19	3.3	3.5	27.7 ± 10.7	0.100	0.369	3.89 ± 0.60
1988 C III]	19	3.3	3.6	34.2 ± 2.4	0.066	0.018	1.29 ± 0.10
1988 Mg II	14	4.4	4.0	25.9 ± 2.6	0.050	0.088	1.36 ± 0.12
1991 1355 Å	22	1.7	1.0	140.0 ± 56.1	0.039	0.390	3.38 ± 0.17
1991 C IV	22	1.7	1.0	283.6 ± 73.7	0.024	0.259	2.17 ± 0.06
1991 He II	22	1.7	1.0	53.6 ± 15.3	0.070	0.275	2.58 ± 0.23
1991 C III]	22	1.7	1.0	54.8 ± 6.0	0.027	0.106	1.50 ± 0.043
1991 Mg II	20	1.5	1.0	51.0 ± 5.0	0.025	0.094	1.39 ± 0.06

¹Continuum and emission-line fluxes are in the same units used in Tables 2–5.

Table 7. Cross-Correlation Results

Line (1)	r_{\max} (2)	τ_{cent}^1 (days) (3)	τ_{peak}^1 (days) (4)
1988 C IV λ 1549	0.882 ± 0.055	$3.44^{+1.42}_{-1.24}$	$3.1^{+2.0}_{-1.1}$
1988 He II λ 1640	0.819 ± 0.078	$3.47^{+1.97}_{-1.61}$	$3.6^{+1.9}_{-3.5}$
1988 C III] λ 1909	0.709 ± 0.107	$6.90^{+4.58}_{-3.83}$	$6.5^{+4.9}_{-3.9}$
1988 Mg II λ 2798	0.883 ± 0.064	$6.83^{+1.74}_{-2.10}$	$6.6^{+2.2}_{-1.6}$
1991 C IV λ 1549	0.965 ± 0.018	$3.28^{+0.83}_{-0.91}$	$3.3^{+0.5}_{-0.8}$
1991 He II λ 1640	0.933 ± 0.034	$2.60^{+1.10}_{-1.21}$	$1.5^{+1.2}_{-1.0}$
1991 C III] λ 1909	0.884 ± 0.048	$3.45^{+1.52}_{-1.22}$	$3.6^{+2.0}_{-2.2}$
1991 Mg II λ 2798	0.925 ± 0.177	$5.35^{+1.87}_{-1.77}$	$4.6^{+2.8}_{-2.5}$

¹ags are in the observed frame.

Table 8. Emission Line Widths

Line (1)	σ_{line} (km s^{-1}) (2)	FWHM (km s^{-1}) (3)
1988 C IV λ 1549 ¹	5698 ± 245	6697 ± 543
1988 He II λ 1640 ²	5013 ± 323	5356 ± 1270
1988 C III] λ 1909	2553 ± 307	2646 ± 745
1988 Mg II λ 2798	2581 ± 179	4823 ± 1105
1991 C IV λ 1549 ¹	5140 ± 113	4858 ± 149
1991 He II λ 1640 ²	4530 ± 92	4597 ± 659
1991 C III] λ 1909	2817 ± 81	6997 ± 1366
1991 Mg II λ 2798	2721 ± 141	6458 ± 1850

¹Based on the shortward side of the line only.

²Based on the longward side of the line only.